The role of iron in the electronic configuration of mixed nickel iron oxides for the OER - Supplementary Information

Christopher Gort[*,1], Gustavo T. Feliciano[2], Alexander A. Auer[2], Bernhard Kaiser[1], Wolfram Jaegermann[1], Jan P. Hofmann[*,1]

[1]Surface Science Laboratory, Department of Materials- and Geosciences, Technical University of Darmstadt, Peter-Grünberg-Straße 4, 64287 Darmstadt, Germany

[2]Max-Planck-Institut für Kohlenforschung, Kaiser-Wilhelm-Platz 1, 45470 Mülheim an der Ruhr, Germany

[*]Corresponding author E-Mail: *hofmann@surface.tu-darmstadt.de*

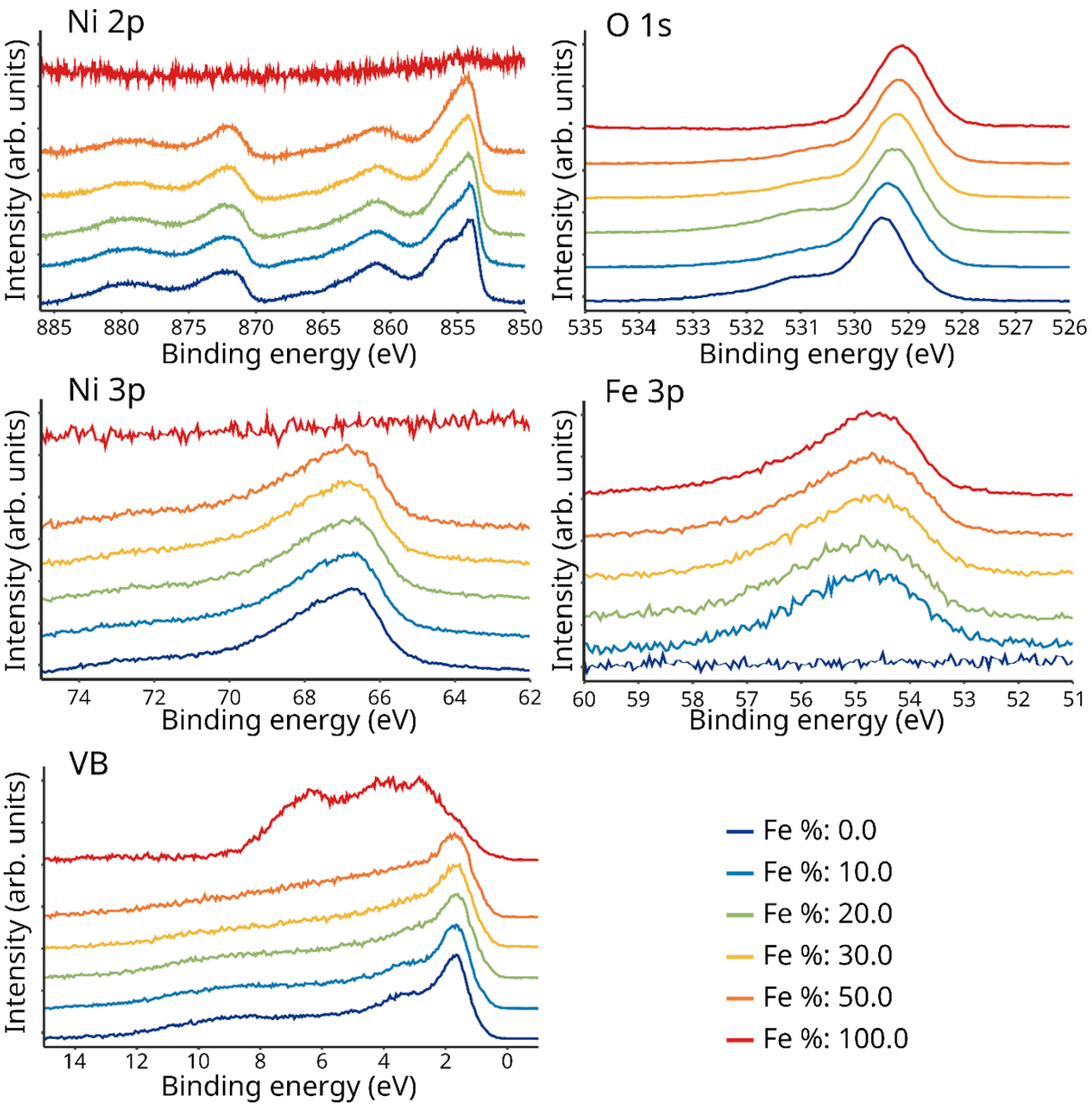

Fig. S 1: Lab based XP spectra of pristine samples

Lab based XP spectra of pristine samples right after deposition and without breaking the vacuum. The above spectra thus represent the pristine state of the samples before they came into contact with ambient air for synchrotron measurements. Spectra intensities are normalized to the interval [0,1], a Shirley type background is subtracted and an offset is added for better comparison.

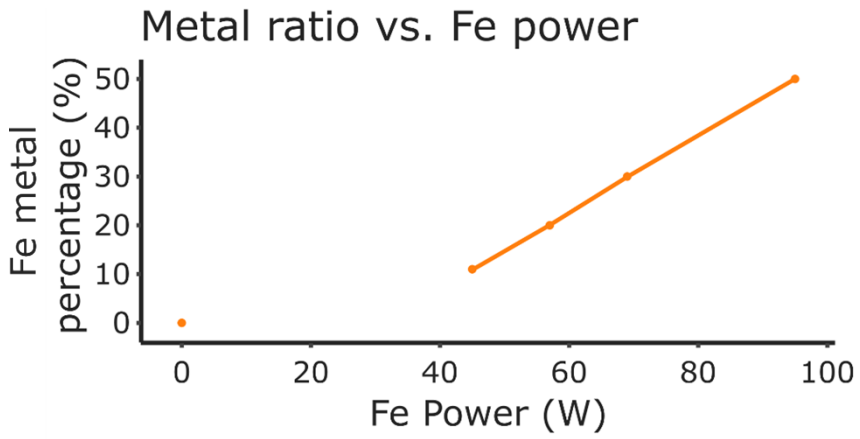

Fig. S 2: iron metal ratio vs. iron RF power

iron metal ratio vs. iron RF power as estimated from area fits to the metal 3p core levels with lab based XPS of the pristine samples directly after deposition.

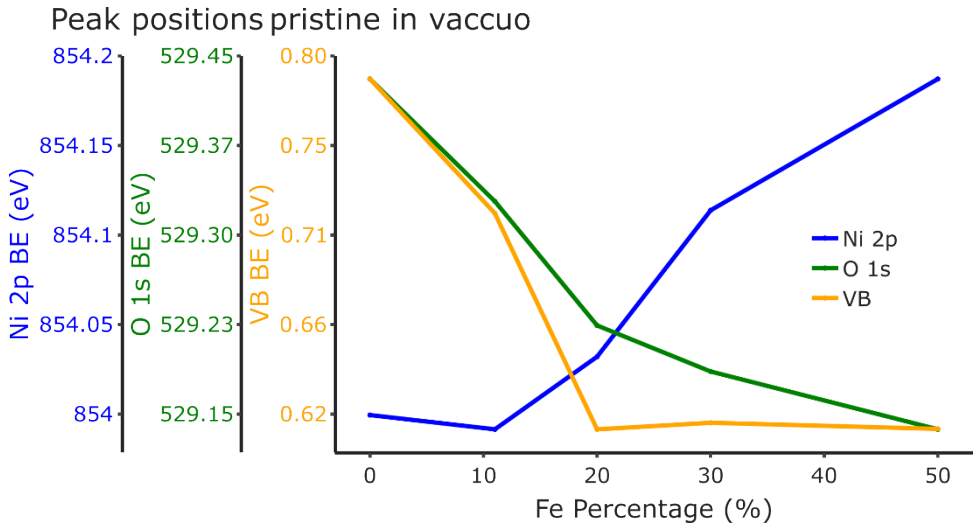

Fig. S 3: pristine in vacuo binding energy positions of Ni 2p, O 1s and VB main peaks.

Binding energy positions of the main peak of the Ni 2p and O 1s core level as well as the valence band edge were fitted according to the procedure described in the experimental section. The Binding energies are plotted against the iron metal content and show a shift of the O 1s level and the valence band maximum to lower energies for increasing iron content.

Basic Sample Report
2/1/2024 3:11:45 PM

QTEGRA

Label: Sample_7_Ni4Fe(OH)x_Chris , #: 16
Analysis started at: 1/10/2024 12:03:48 PM
Standard DF: 1

Analyte (Measure Mode)	Concentration average
Al 167.079 (Aqueous-Axial-iFR)	0.001 ppm
Pt 203.646 (Aqueous-Axial-iFR)	N/A
Pt 214.423 (Aqueous-Axial-iFR)	N/A
Ni 221.647 (Aqueous-Axial-iFR)	1.035 ppm
Co 228.616 (Aqueous-Axial-iFR)	0.000 ppm
Ni 231.604 (Aqueous-Axial-iFR)	1.035 ppm
Co 237.862 (Aqueous-Axial-iFR)	0.000 ppm
Fe 238.204 (Aqueous-Axial-iFR)	0.251 ppm
Co 238.892 (Aqueous-Axial-iFR)	-0.010 ppm
Fe 239.562 (Aqueous-Axial-iFR)	0.242 ppm
Mn 257.610 (Aqueous-Axial-iFR)	0.001 ppm
Mn 259.373 (Aqueous-Axial-iFR)	0.001 ppm
Fe 259.940 (Aqueous-Axial-iFR)	0.246 ppm
Mn 260.569 (Aqueous-Axial-iFR)	0.001 ppm
Pt 265.945 (Aqueous-Axial-iFR)	N/A
Cr 267.716 (Aqueous-Axial-iFR)	0.002 ppm
Cr 283.563 (Aqueous-Axial-iFR)	0.002 ppm
Cr 284.325 (Aqueous-Axial-iFR)	0.001 ppm
Al 308.215 (Aqueous-Axial-iFR)	-0.011 ppm
Al 309.271 (Aqueous-Axial-iFR)	-0.014 ppm

Fig. S 4: ICP-OES results of an example sample

ICP-OES results for a sample with a target metal ratio of 1:4 as prepared by co-sputtering and estimated with XPS of TM 3p orbitals. The ICP-OES results match the XPS estimations with a metal ratio of 0.248 : 1.035

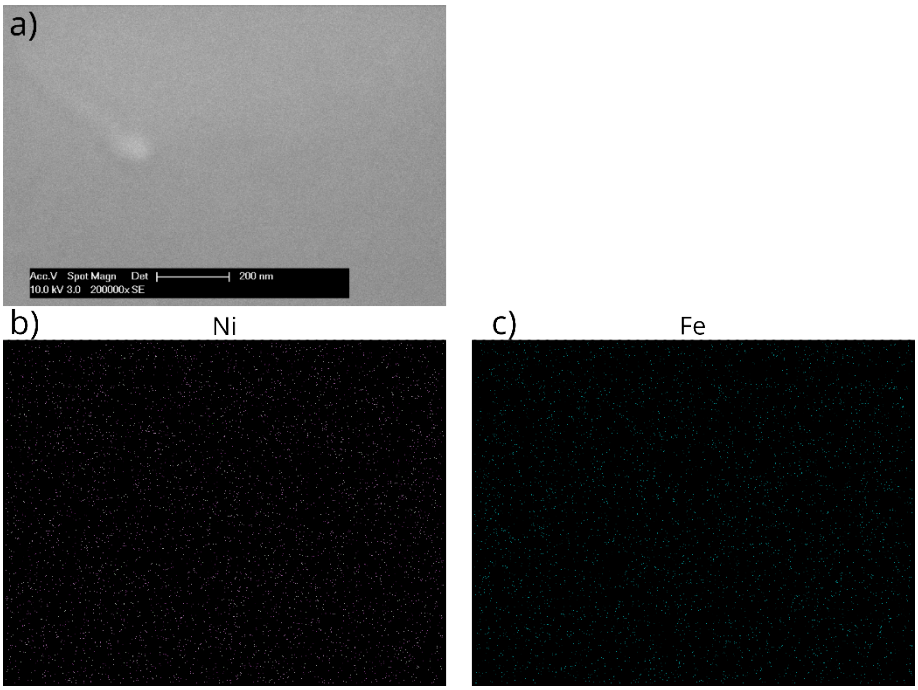

Fig. S 5: SEM + EDX image of an example sample

a) SEM and b) & c) EDX images of the Fe 30% synchrotron sample after electrochemical treatment. The SEM zoom in a) shows a speck of dust, on which the optics were focused, next to an otherwise smooth surface. On a scale of 200nm the sample shows no phase segregation of nickel and iron, but rather a homogeneous distribution of both. Note: the EDX data points are sparsely pixelated and can best be seen when zooming the image/document.

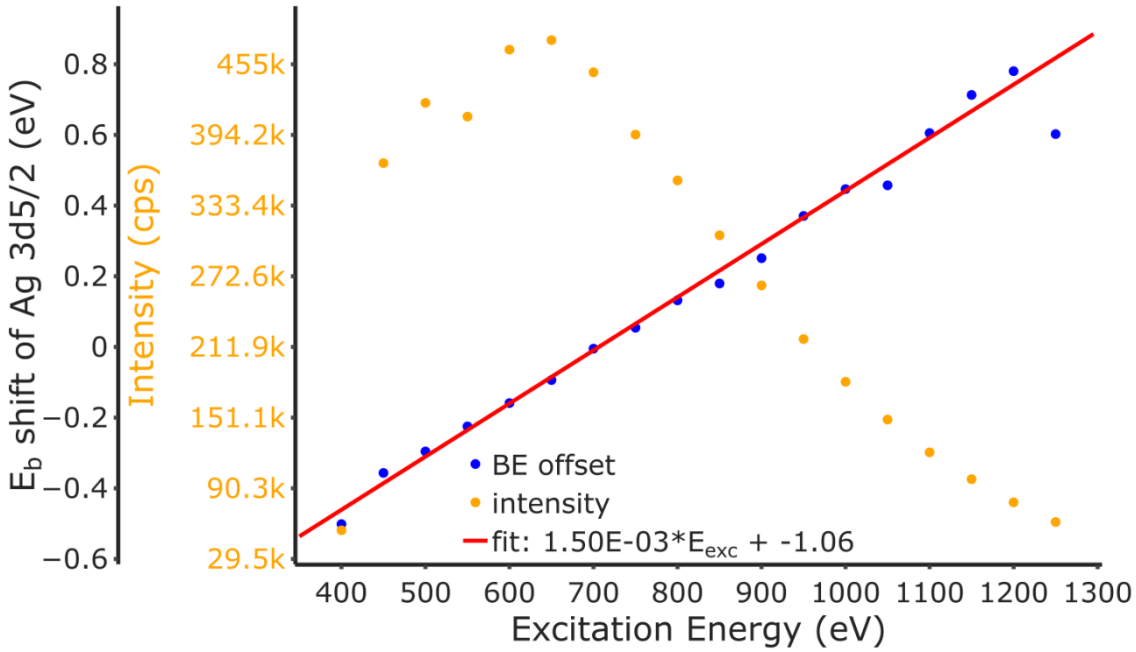

Fig. S 6: characterization of the beamline on the Ag 3d5/2 signal of a sputter cleaned silver sample.

The Ag 3d5/2 binding energy offset vs. literature value (blue dots) and the intensity of the Ag 3d5/2 peak (orange dots) in dependence of the excitation energy set at the synchrotron monochromator at beam line PM3. The red curve shows a linear fit to the energy offset of the Ag 3d5/2 peak position.

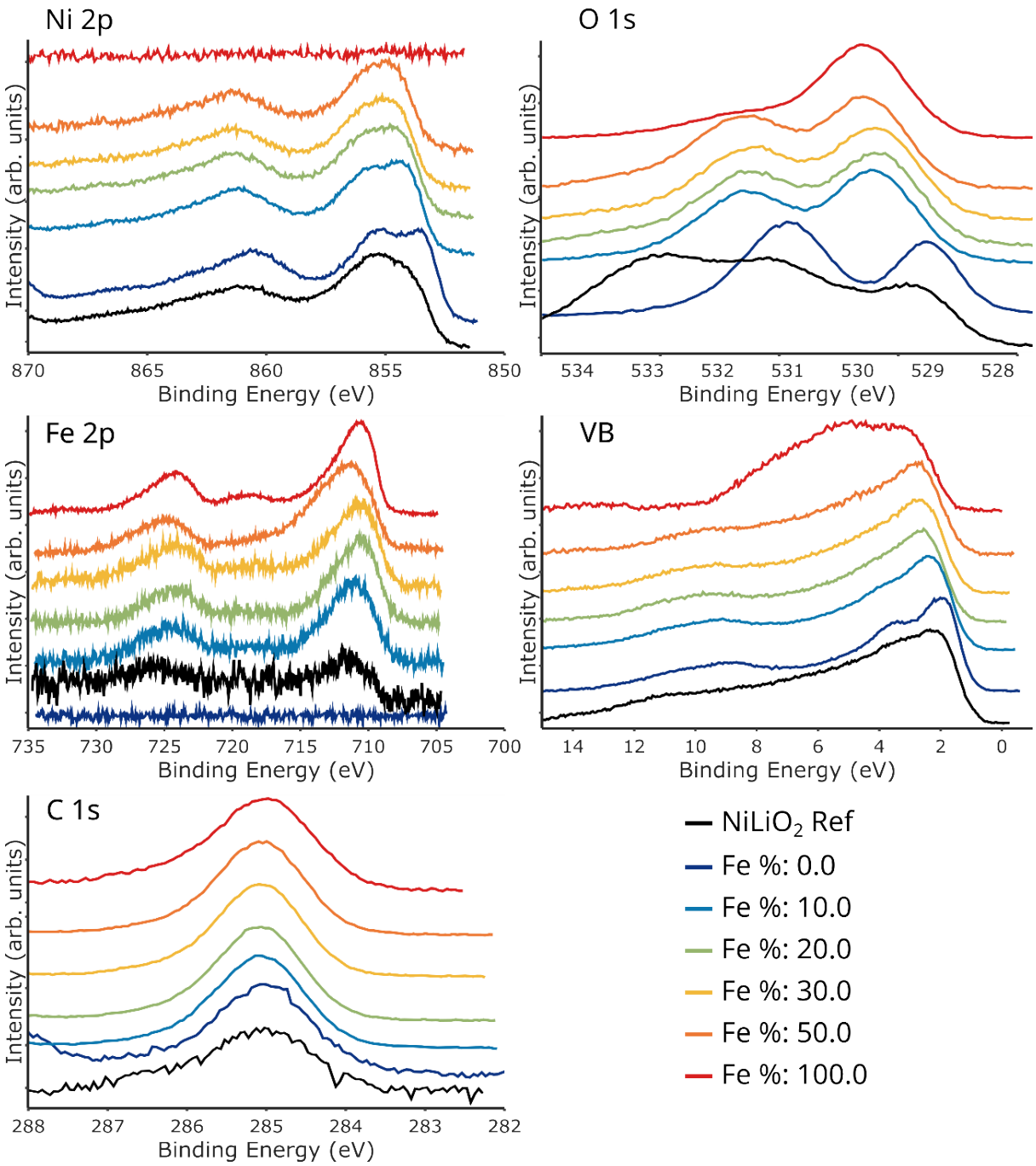

Fig. S 7: Synchrotron XPS at before activation at E_{kin} = 400 eV of primary photoelectrons.

Synchrotron XPS at before activation at E_{kin} = 400 eV of primary photoelectrons. Spectra were calibrated to give a binding energy of 285 eV for the C-C peak of adventitious carbon. Furthermore, spectra intensities are normalized to the interval [0,1], a Shirley type background is subtracted and an offset is added for better comparison. Exception for the background correction are the Ni 2p core levels where the secondary electron edge made a reasonable fit impractical.

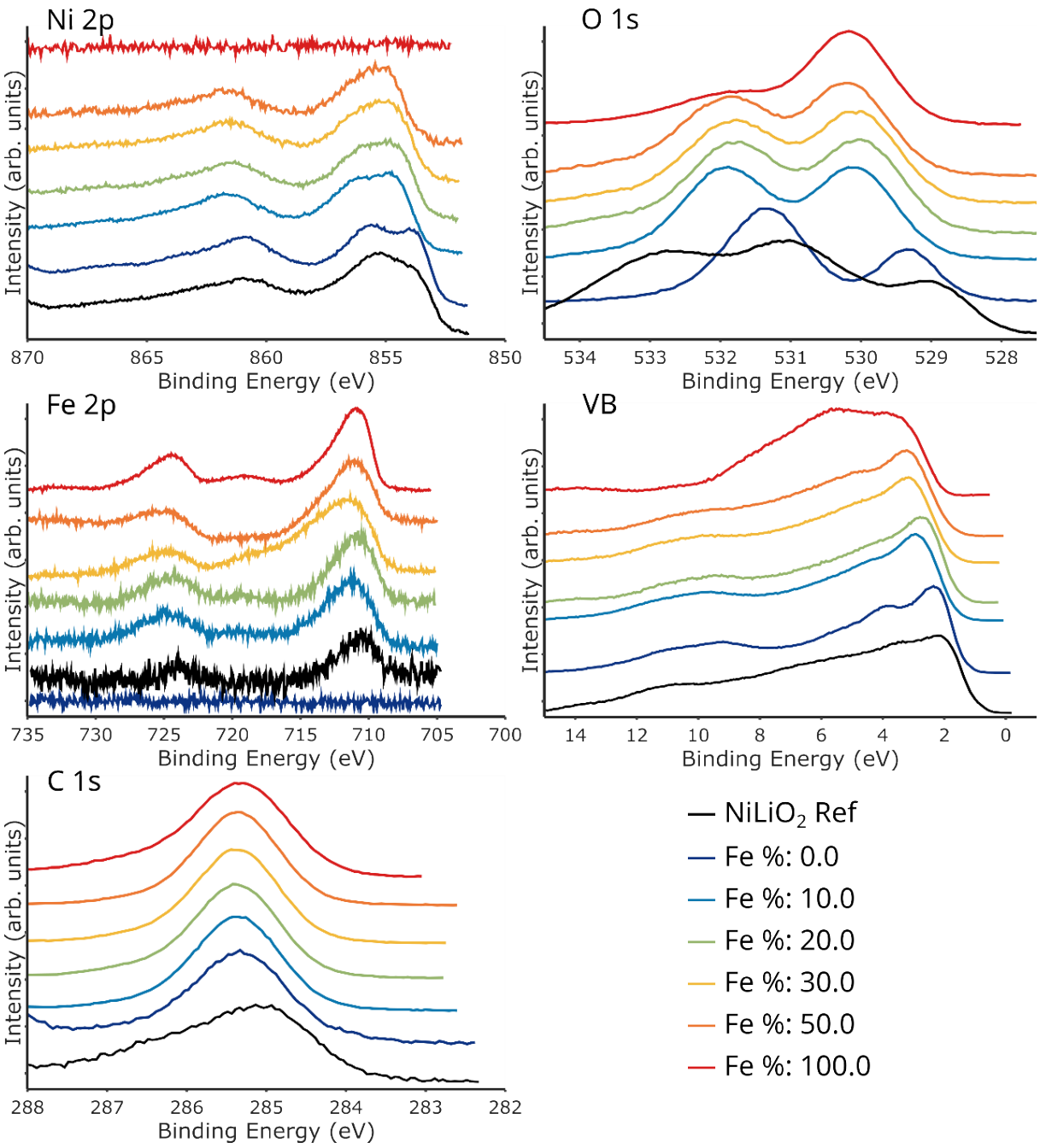

Fig. S 8: Synchrotron XPS at before activation at E_{kin} = 200 eV of primary photoelectrons.

Synchrotron XPS at before activation at E_{kin} = 200 eV of primary photoelectrons. Spectra were calibrated to give a binding energy of 285 eV for the C-C peak of adventitious carbon. Furthermore, spectra intensities are normalized to the interval [0,1], a Shirley type background is subtracted and an offset is added for better comparison. Exception for the background correction are the Ni 2p core levels where the secondary electron edge made a reasonable fit impractical.

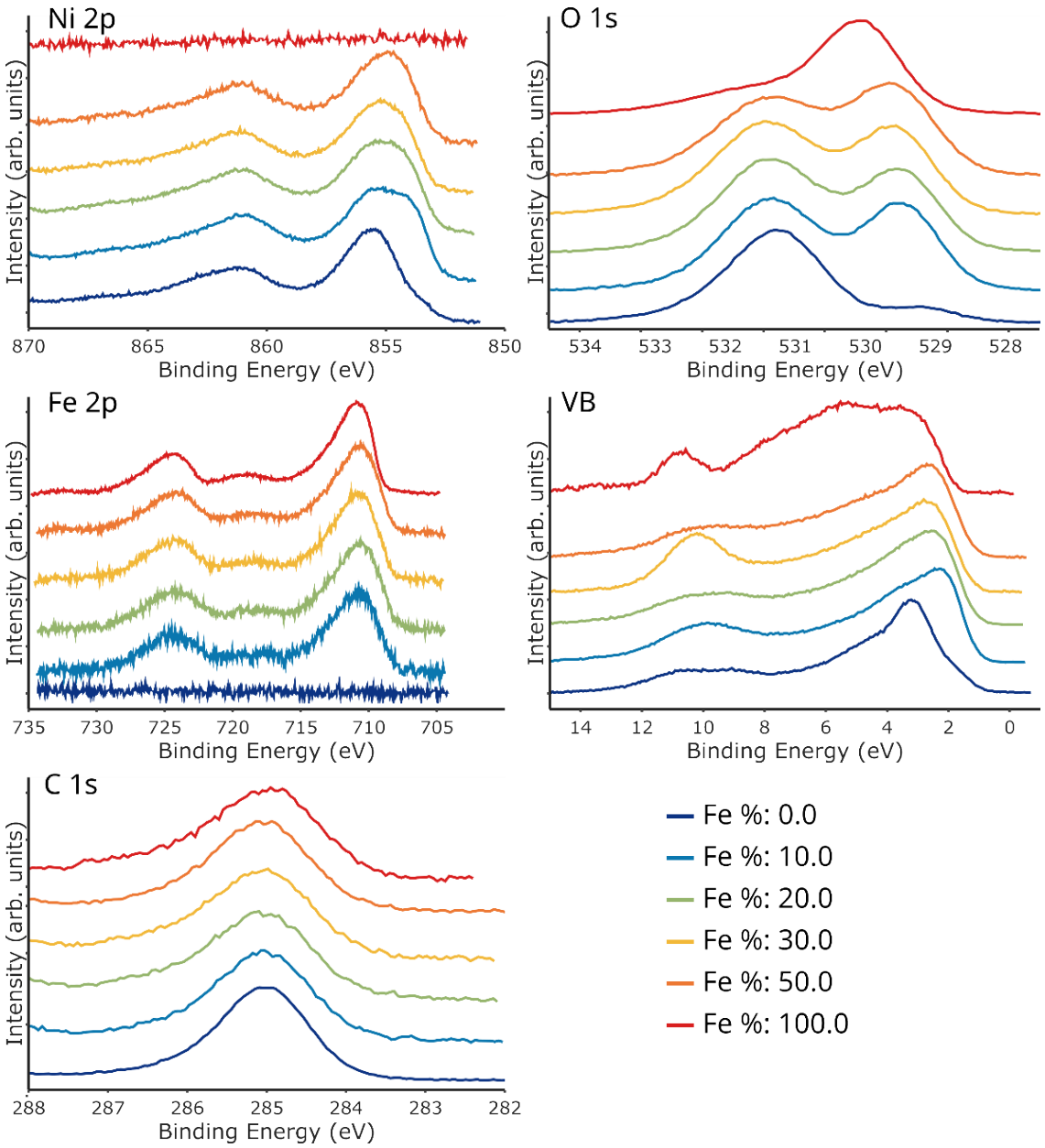

Fig. S 9: Synchrotron XPS at after activation at E_{kin} = 400 eV of primary photoelectrons

Synchrotron XPS at after activation at E_{kin} = 400 eV of primary photoelectrons. Spectra were calibrated to give a binding energy of 285 eV for the C-C peak of adventitious carbon. Furthermore, spectra intensities are normalized to the interval [0,1], a Shirley type background is subtracted and an offset is added for better comparison. Exception for the background correction are the Ni 2p core levels where the secondary electron edge made a reasonable fit impractical.

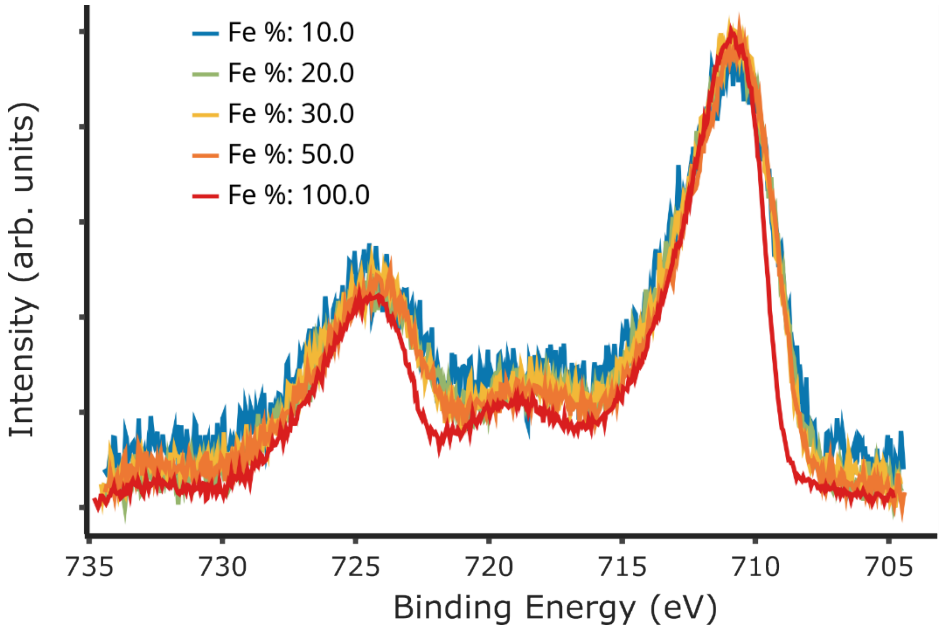

Fig. S 10: Fe 2p synchrotron XP spectra after activation.

Fe 2p synchrotron spectra after activation measured at 400 eV kinetic energy of primary photoelectrons (1105 eV excitation energy) to avoid overlap with Ni Auger lines. A Shirley type background was subtracted and the spectra were normalized to the interval [0,1]. Except for the spectrum of pure FeOx all other spectra are nearly identical. Spectra were calibrated to give a binding energy of 285 eV for the C-C peak of adventitious carbon.

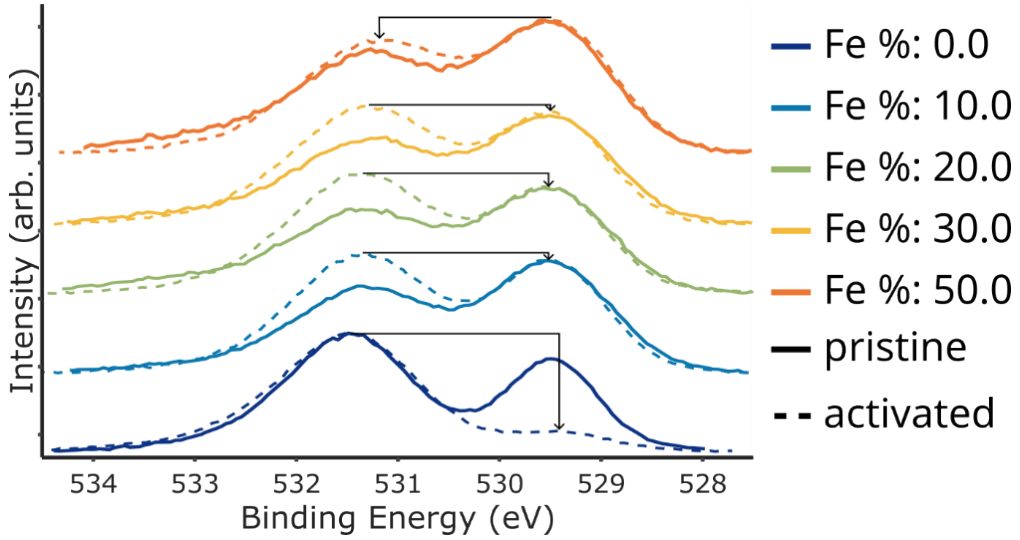

Fig. S 11: O 1s XPS activation comparison

O 1s spectra of samples before and after activation. Visible is the increase of the hydroxide peak at around 531.5 eV and the simultaneous decrease of the lattice oxide peak at around 529.3 eV. Arrows indicate that for growing iron content the transformation to hydroxide decreases. Spectra were calibrated to give a binding energy of 529.3 eV for the lattice oxygen peak for better comparison of the changes in hydroxylation.

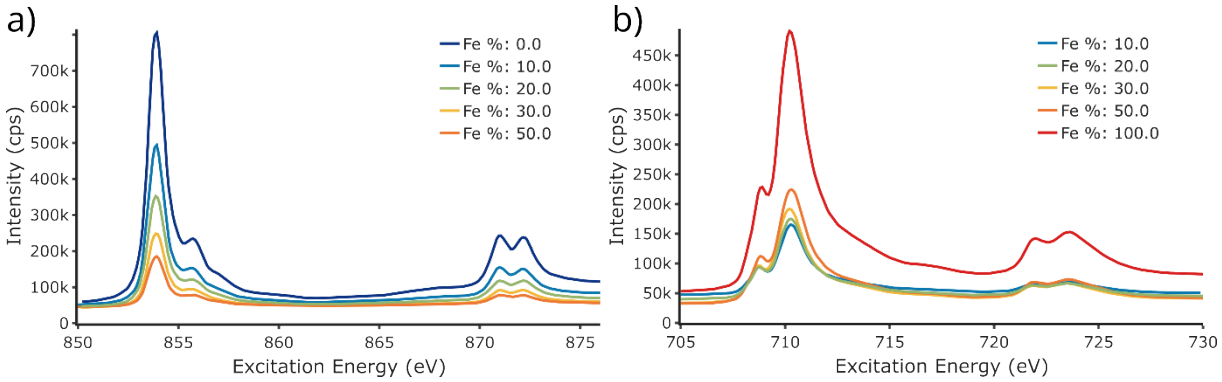

Fig. S 12: metal L-edge spectra before activation

NEXAFS measurements of samples before any treatment. Data plotted as is, without any scaling. a) Ni L-edge, b) Fe L-edge. With increasing iron content the Ni L-edge signal is decreasing and vice versa the Fe L-edge is increasing.

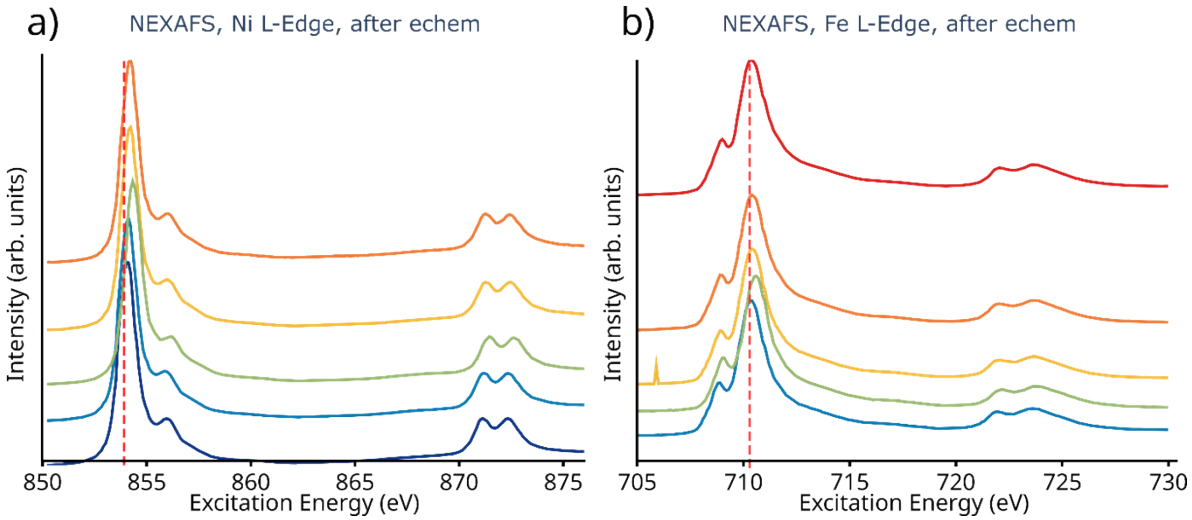

Fig. S 13: metal L-edge spectra after activation

NEXAFS measurements on metal L-edges after electrochemical activation. Dashed lines indicate the excitation energies used for resPES. The red dashed line shows the excitation energy at the XAS absorption edge of the main peak used for the resPES plots in the main manuscript.

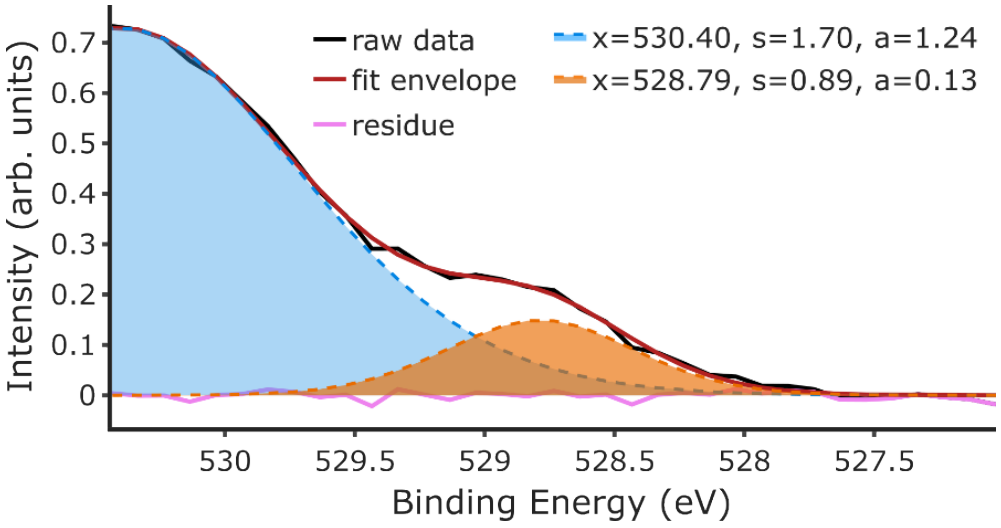

Fig. S 14: Fit procedure for estimating the hole state area.

Procedure for estimating the pre-edge peak area. Two gaussian peak are fitted to the O K-edge and the amplitude of the smaller one is taken as the pre-edge peak area.

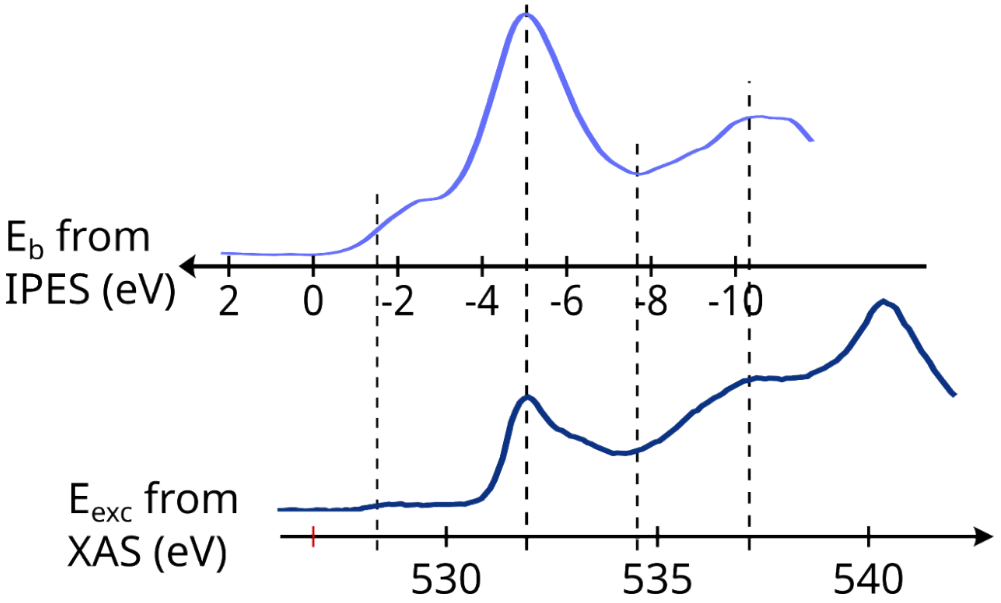

Fig. S 15: Calibration of NEXAFS data to the Fermi level.

NEXAFS vs. IPES comparison for the NiO sample. The same empty Ni 3d – O 2p state is at 5 eV IPES and 532 eV NEXAFS. The dashed lines indicate the energy position from IPES that are used to calibrate the energy of the NEXAFS axis for main Fig. 5. The red dash line in the lower plot indicates the zero point of the NEXAFS spectrum with respect to EF.

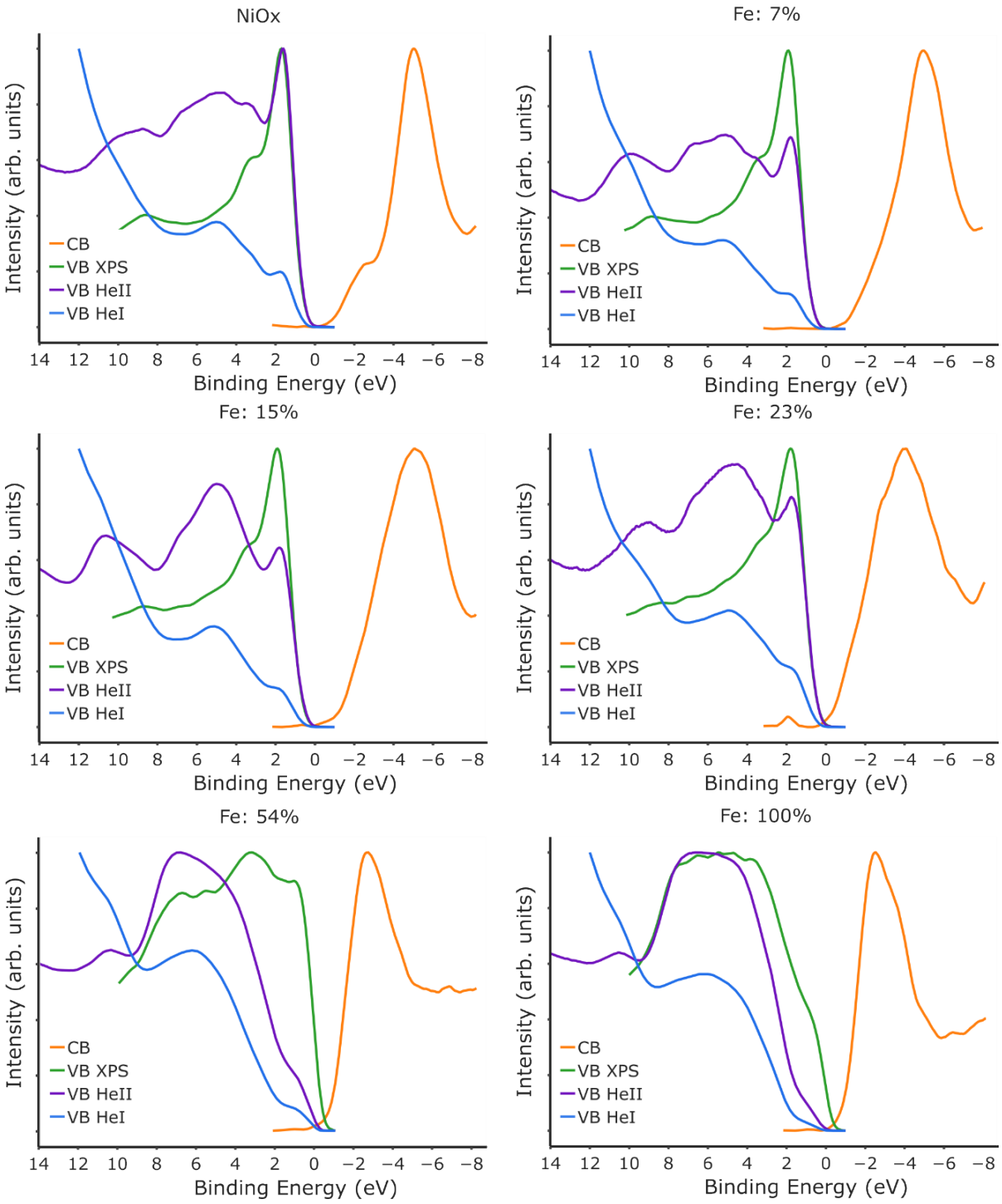

Fig. S 16: UPS, IPES and XPS of the valence bands.

BIS IPES, XPS and UPS (He I: 21.2 eV and He II: 40.8 eV excitation energy) measurements on a set of samples not used in the synchrotron experiment series. The substrate was silicon with a native oxide layer and a chromium layer instead of the titanium substrate used in the main manuscript. Wear of the sputter target lead to slightly different metal concentrations compared to the synchrotron sample set. The Fe 54% and Fe 100% samples additionally showed metallic species in the Ni 2p XP spectra, probably due to excessive oxygen consumption in this sputter parameter region. They are still shown for the sake of completeness.

Illustrations of the systems studied in the DFT calculations

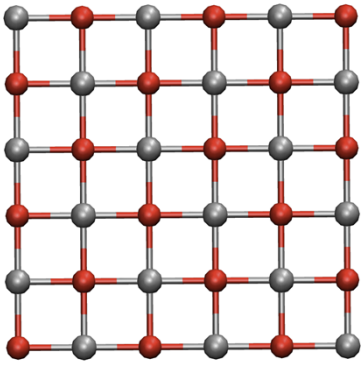

$Ni_{54}O_{54}$ (oxide)

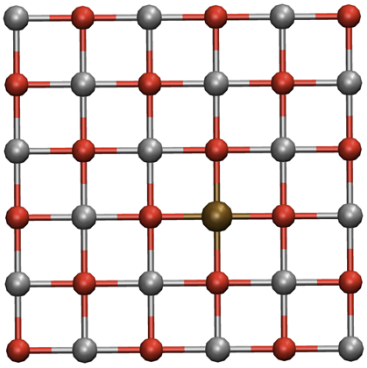

$Ni_{53}FeO_{54}$ (oxide)

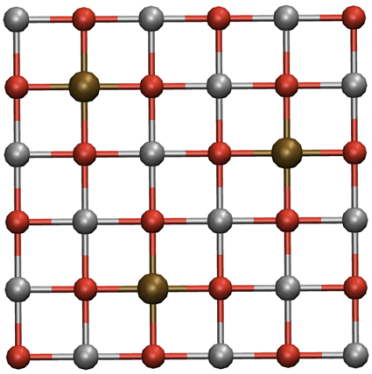

$Ni_{51}Fe_3O_{54}$ (oxide)

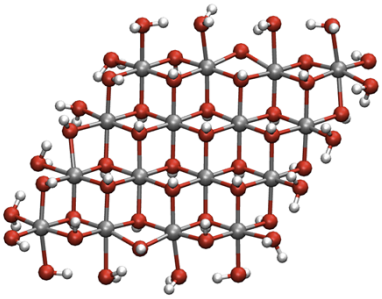

$Ni_{16}O_{48}H_{64}$
(hydroxide)

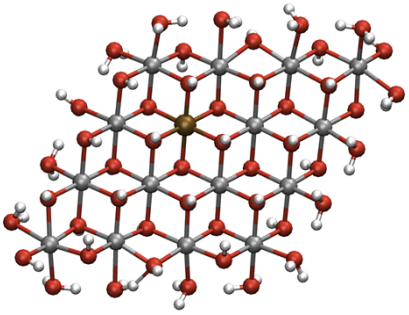

$Ni_{15}FeO_{48}H_{64}$
(hydroxide)

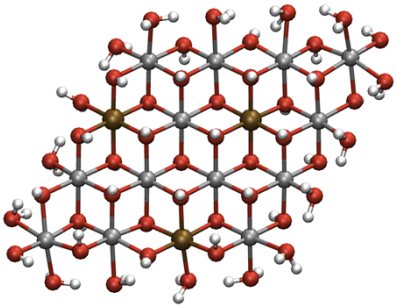

$Ni_{13}Fe_3O_{48}H_{64}$
(hydroxide)

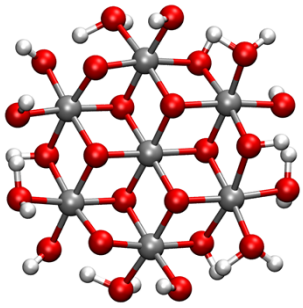

$Ni_7O_{24}H_{22}$
(oxyhydroxide)

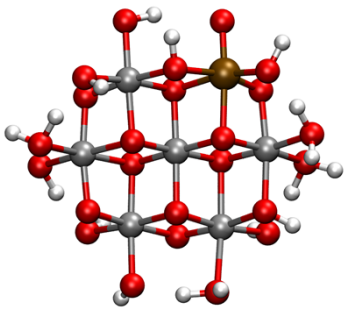

$Ni_6FeO_{24}H_{19}$
(oxyhydroxide)

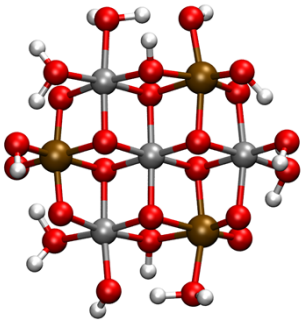

$Ni_4Fe_3O_{24}H_{18}$
(oxyhydroxide)

Additional Computational Details

The calculations were performed using the B3LYP density functional[1–3] and def2-SVP basis-set[4,5]. All calculations were performed using the ORCA 6 program[6,7]. The DOS data was generated using Mulliken partition scheme, with a Lorentzian broadening of 0.2 eV, through the MultiWfn program[8,9]. The data of core position coordinates is given in the "DFT calculation XYZ coordinates.txt" file of the supplementary information.

In this work, we considered nickel and iron modified nickel oxide materials in different phases, representing three possible different stages of the material transformation, in terms of oxidation and deprotonation events:

(i) oxide materials, where we employed a multiscale QM/MM approach. Three layers of NiO, with 36 atoms each (the quantum charge (QC) region), are described using electronic structure methods. This system is then embedded in a larger NiO cubic supercell of 27000 atoms (the partial charge (PC) region), where the surrounding Ni and O atoms are treated as point charges (+2 and -2, respectively). A buffer region of 0.28 nm between these two regions is also considered (the effective core potential (ECP) region), in order to smoothen the discontinuity in the charge distribution at the interface and avoid spurious interactions that can affect the calculation. The NiFeO material is generated from the same protocol, but replacing three Ni atoms in the central QC layer with Fe atoms, as far apart as possible.

(ii) hydroxide materials, the structure is protonated at all oxygens with the highest amount of protons possible, and the system is embedded in a polarizable continuum media for implicit solvation simulation, with the corresponding dielectric constant of water[10,11]. In this case, the dispersion correction with Becke-Johnson damping was applied[12]

(iii) oxyhydroxide materials, which are obtained optimizing protonation and charge state, according to a protocol developed in the group for taking into account pH and potential conditions for OER, also with implicit solvation[13,14]. In this case, the structure is obtained for U-1.6V and pH 14. The dispersion correction with Becke-Johnson damping was applied[12]

Electrochemical Activation Routine

For activation we used a setup consisting of a PalmSens 4 potentiostat and a Zahner PECC cell with 0.1 M KOH from Roth GmbH. The electrochemical routine consisted of an initial OCP measurement and a CV to measure equilibrium conditions and the first behavior after polarization. After this, small interval CVs below the potential window of the Ni redox wave were performed with varying scan rates to estimate the electrochemical surface area. Next EIS measurements were performed to gauge system resistances. The heart of the activation routine consisted next of three CV measurements in the interval 1.1-1.8 V vs. RHE to transform the initial oxides into hydroxides via the Ni+2/+3 redox wave and to estimate OER performance. The three consecutive activation CVs were performed with 5 cycles @ 5 mV/s, 50 cycles @ 50 mV/s and finally again 5 cycles @ 5mV/s scan rates. After the activation CVs we repeated the small interval CVs and the EIS measurements to probe the phases after transformation.

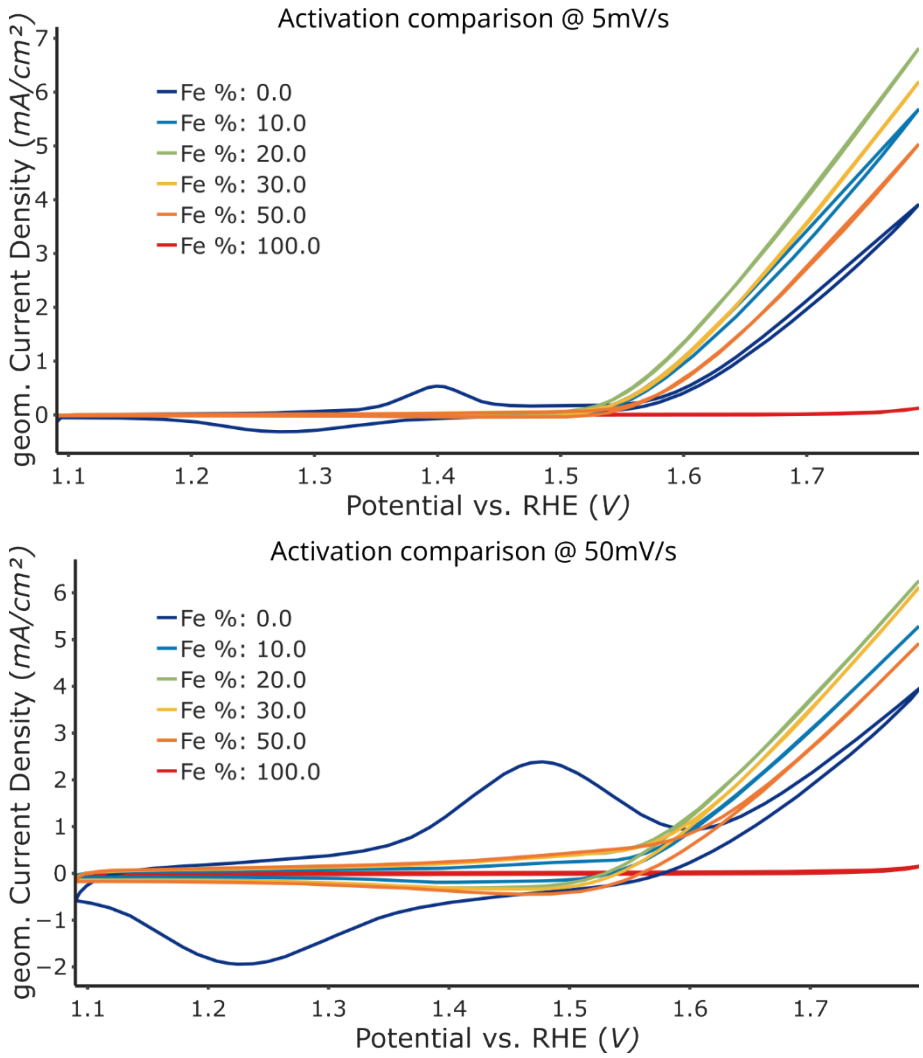

Fig. S 17: Cyclic voltammetry for sample activation

Cyclic voltammetry curves to activate the samples for 5 mV/s and 50 mV/s. The OER onset starts around 1.55 V and OER currents increase with increasing iron content up to a percentage of 20 %. For higher iron contents activity is decreasing and the pure iron oxide sample is nearly OER inactive. For the faster, 50 mV/s scan rate measurements the redox waves of the $Ni^{2+/3+}$ transition are enhanced.

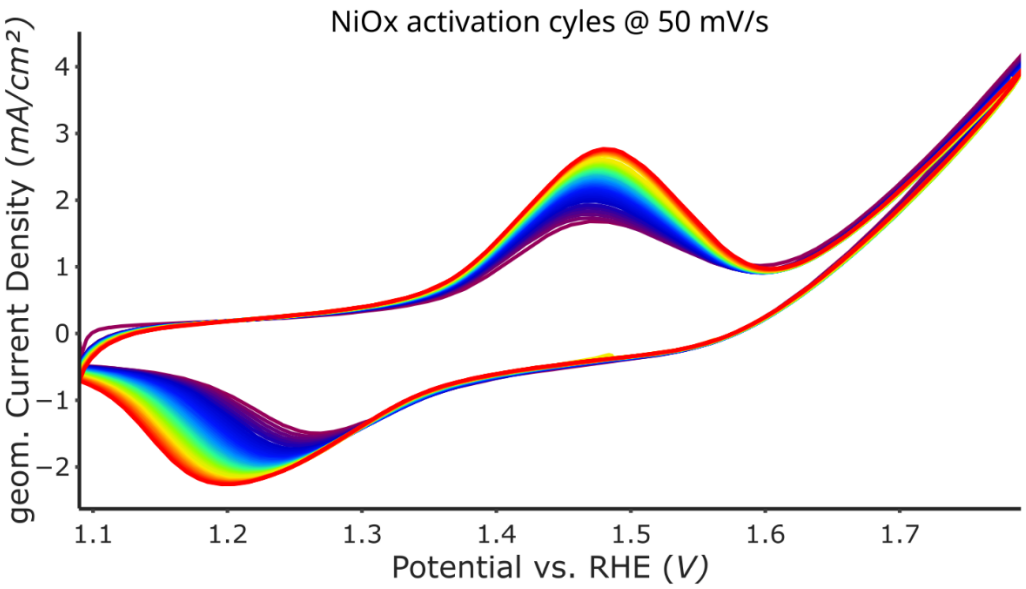

Fig. S 18: Redox wave area increase with cycling for NiO

Zoom in to the redox wave for NiOx. The color code here indicates cycles passed with cycle number increasing from violet (1st cycle) over blue to red (50th cycle). For the NiO sample plotted here the increase in the redox wave area is clearly noticeable in contrast to samples with iron.

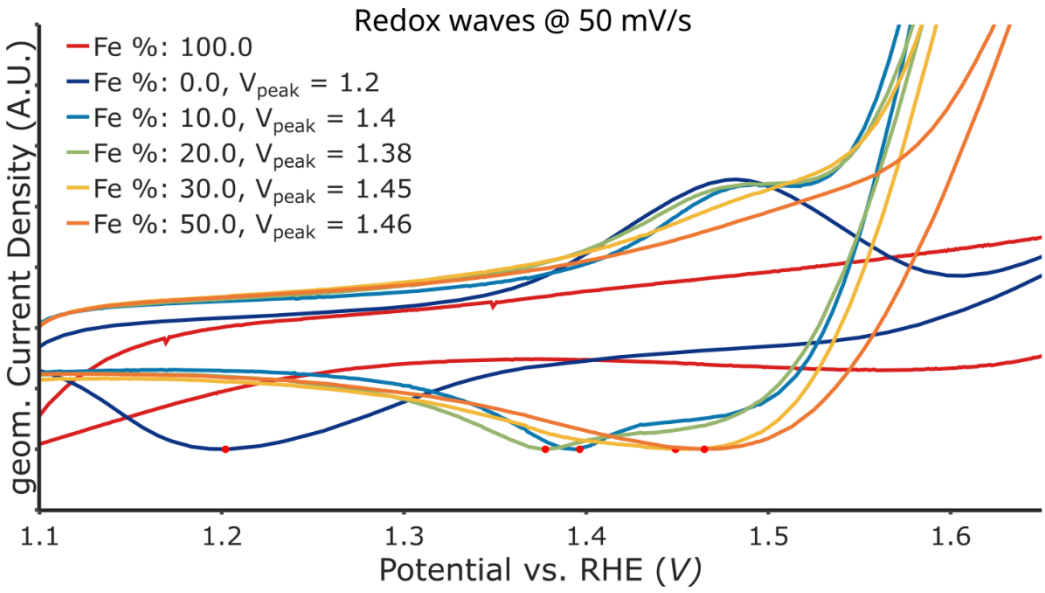

Fig. S 19: Potential shift of the nickel redox wave with iron content

Zoom in to the cathodic redox wave parts. For estimation of the redox wave center, the cathodic redox peak was chosen, since the anodic one was obscured by the OER for higher iron contents. The currents are normalized to the cathodic redox wave peak. The red dots indicate the peak maxima of the redox waves which shift to more anodic values with increasing iron content.

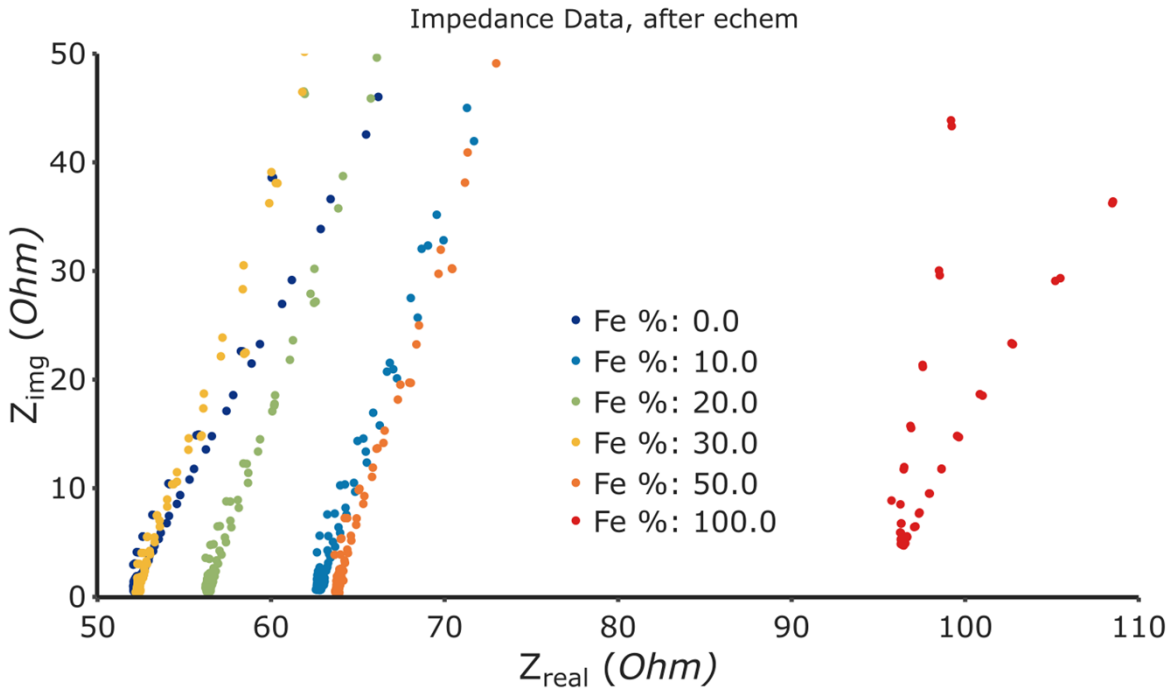

Fig. S 20: Impedance measurements after electrochemical activation

Impedance measurements after electrochemical activation at a DC voltage of 1.0 V vs RHE. The minima of the data sets close to the x-axis resemble the high frequency resistances which reflect series resistances in the system.

References

[1] A. D. Becke, *J. Chem. Phys.* **1993**, *98*, 5648.
[2] C. Lee, W. Yang, R. G. Parr, *Physical review. B, Condensed matter* **1988**, *37*, 785.
[3] S. H. Vosko, L. Wilk, M. Nusair, *Can. J. Phys.* **1980**, *58*, 1200.
[4] F. Weigend, R. Ahlrichs, *Physical chemistry chemical physics PCCP* **2005**, *7*, 3297.
[5] F. Weigend, *Physical chemistry chemical physics PCCP* **2006**, *8*, 1057.
[6] F. Neese, *Wiley Interdisciplinary Reviews: Computational Molecular Science* **2012**, *2*, 73.
[7] F. Neese, F. Wennmohs, U. Becker, C. Riplinger, *J. Chem. Phys.* **2020**, *152*, 224108.
[8] T. Lu, F. Chen, *Journal of Computational Chemistry* **2012**, *33*, 580.
[9] T. Lu, *J. Chem. Phys.* **2024**, *161*.
[10] M. Garcia-Ratés, F. Neese, *Journal of Computational Chemistry* **2020**, *41*, 922.
[11] V. Barone, M. Cossi, *The Journal of Physical Chemistry A* **1998**, *102*, 1995.
[12] S. Grimme, J. Antony, S. Ehrlich, H. Krieg, *J. Chem. Phys.* **2010**, *132*, 154104.
[13] K. Bhattacharyya, C. Poidevin, A. A. Auer, *J. Phys. Chem. C* **2021**, *125*, 4379.
[14] K. Bhattacharyya, A. A. Auer, *J. Phys. Chem. C* **2022**, *126*, 18623.